Mon. Not. R. Astron. Soc. **000**, 1–?? (2014) Printed 5 November 2014 (MN LATEX style file v2.2)

Search for PAHs in the Perseus molecular cloud with the Green Bank Telescope

Yacine Ali-Haïmoud[1,2⋆], Laura M. Pérez[3]†, Ronald J. Maddalena[4] and D. Anish Roshi[5]
1 *Department of Physics and Astronomy, Johns Hopkins University, Baltimore MD 21218*
2 *School of Natural Sciences, Institute for Advanced Study, Einstein Drive, Princeton, NJ 08540, USA*
3 *National Radio Astronomy Observatory, P.O. Box O, Socorro, NM 87801, USA*
4 *National Radio Astronomy Observatory, P.O. Box 2. Green Bank, WV 24944, USA*
5 *National Radio Astronomy Observatory, Green Bank and Charlottesville, VA 22903, USA*

arXiv:1411.0691v1 [astro-ph.GA] 3 Nov 2014

5 November 2014

ABSTRACT

Polycyclic Aromatic Hydrocarbons (PAHs) are believed to be the small-size tail of the interstellar carbonaceous dust grain population. Their vibrational emission is the most widely accepted source of the aromatic near-infrared features, and their rotational radiation is a likely explanation for the dust-correlated anomalous microwave emission (AME). Yet, no individual interstellar PAH molecule has been identified to date. It was recently recognised that quasi-symmetric planar PAHs ought to have a well identifiable comb-like rotational spectrum, and suggested to search for them in spectroscopic data with matched-filtering techniques. We report the results of the first such search, carried out with the Green Bank Telescope, and targeting the star-forming region IC348 in the Perseus molecular cloud, a known source of AME. Our observations amounted to 16.75 hours and spanned a 3 GHz-wide band extending from 23.3 to 26.3 GHz. Using frequency switching, we achieved a sensitivity of 0.4 mJy per 0.4 MHz channel (1σ). The non-detection of comb-like spectra allowed us to set upper bounds on the abundance of specific quasi-symmetric PAH molecules (specified uniquely by their moments of inertia) of approximately 0.1% of the total PAH abundance. This bound generically applies to PAHs with approximately 15 to 100 carbon atoms.

Key words: ISM: dust, molecules, lines and bands

1 INTRODUCTION

It is nowadays widely accepted that Polycyclic Aromatic Hydrocarbons (PAHs) are ubiquitous in the interstellar medium (ISM). These large and very stable molecules constitute the small-size tail of the carbonaceous dust grain population. They are important actors in the thermal and chemical balance of the ISM (Tielens 2008). The mid-infrared (IR) aromatic features at 3-20 μm, main evidence for PAHs, are believed to result from their vibrational emission following stochastic heating by ultraviolet (UV) photons. Their strength implies that a few percent of the interstellar carbon is locked in these molecules (Allamandola et al. 1989). The dust-correlated "anomalous microwave emission" (AME, Leitch et al. 1997), at a few tens of GHz, is most likely rotational emission from PAHs ("spinning dust", Draine & Lazarian 1998). Finally, electronic transitions in PAHs could be the explanation for some of the diffuse interstellar bands (DIBs) observed in the optical and UV (Salama et al. 2011).

Despite its three decades of existence, the PAH hypothesis still lacks an ultimate piece of evidence: the unambiguous identification of specific PAH molecules in space. Such a detection would bring a definitive end to lingering disputes over the nature of the carriers of mid-IR aromatic features (Kwok & Zhang 2011; Li & Draine 2012; Kwok & Zhang 2013; Yang et al. 2013). The search for specific PAHs in space is, however, a challenging task. The aromatic IR bands, cornerstone of the PAH hypothesis, arise from nearest-neighbour C–H and C–C vibrations; as a result, they cannot be used to identify specific PAH molecules in space. In fact, the observed mid-IR spectra can be reproduced by mixtures of a few tens of different PAH species, but the exact composition of the mixtures is not critical (Rosenberg et al. 2014).

⋆ yacine@jhu.edu
† L. M. Pérez is a Jansky Fellow of the National Radio Astronomy Observatory

© 2014 RAS

The far-infrared regime probes the lowest energy modes corresponding to the overall bending of the skeleton, and could provide a successful avenue to identify specific PAHs (Mulas et al. 2006). However these modes carry only a small fraction of the total radiated energy and their contrast with the underlying continuum is expected to be low (Tielens 2008), which has impeded their detection so far. UV and optical spectroscopy has also been used to search for specific PAHs through their electronic transitions, which has allowed to set upper bounds on the abundance of a few specific PAHs, but not lead to any unambiguous detection yet (Gredel et al. 2011; Galazutdinov et al. 2011; see however Iglesias-Groth et al. 2008, 2010, 2012 for tentative detections of naphtalene and anthracene towards the Perseus molecular cloud).

Rotational spectroscopy is a prime tool in the identification of interstellar molecules and the measurement of their abundances, and has obviously been suggested for interstellar PAHs, though rather timidly (Hudgins et al. 2005; Tielens 2008; Hammonds et al. 2011). To date however, only the bowl-shaped corannulene molecule ($C_{20}H_{10}$) has been searched for with this technique, without success (Lovas et al. 2005; Thaddeus 2006; Pilleri et al. 2009). The reasons for the scarcity of works using or even suggesting this technique are twofold. First, there could be a large number of PAH molecules and their individual spectra could be lost in the forest of their combined emission. Second, PAHs are large, generally triaxial molecules, unlike the very special polar and symmetric corannulene molecule. One may therefore a priori expect their rotational emission to be complex and diluted over a very large number of weak lines.

Recently, one of us argued that the prospects of rotational spectroscopy of PAHs may not be so bleak (Ali-Haïmoud 2014, hereafter AH14). First, one can reasonably expect that a few highly symmetric and stable "grand PAHs" could be more fit to survive the harsh ISM conditions and as a result are over-abundant (Tielens 2013). Secondly, even though triaxiality is unavoidable if a planar PAH is to have a permanent dipole moment, the degree of asymmetry need not be large, and the resulting rotational spectrum may still remain relatively simple. In particular, quasi-symmetric nitrogen-substituted PAHs[1], strongly polar and likely common in the ISM (Hudgins et al. 2005), ought to have a well-identifiable "comb"-like rotational spectrum. In addition to being less diluted, the simple shape of the spectrum allows for the use of matched-filtering techniques, resulting in an enhanced sensitivity. Furthermore, one can undertake blind searches of a priori unknown molecules by scanning over comb spacings, without the need for precise and extensive quantum-mechanical calculations or laboratory measurements of their rotational constants.

In this paper we describe our search for quasi-symmetric interstellar PAHs (we show in Figs. 1 and 2 explicit examples of PAHs that do or do not qualify as quasi-symmetric). We rely on rotational spectroscopy and matched filtering, using data taken with the Robert C. Byrd Green Bank Telescope (GBT)[2]. We have targeted the Perseus molecular cloud, a known region of AME (Tibbs et al. 2013), which, if it is indeed spinning dust radiation, is just the collective rotational emission from PAHs. Our observations have reached a sensitivity of 0.4 mJy per 0.4 MHz channel across a 3 GHz total bandwidth. This sensitivity was not enough to detect any comb-like spectrum in our data, but we could set upper bounds on the fractional abundance of specific quasi-symmetric PAHs, assuming the observed AME in Perseus is primarily due to spinning dust emission.

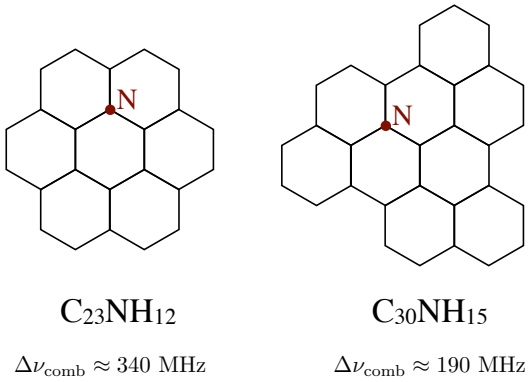

Figure 1. Examples of nitrogen-substituted symmetric PAHs which remain quasi-symmetric after substitution, in the sense that their two smallest moments of inertia differ by less than a few percent. Such molecules are the target of this search. $\Delta\nu_{\rm comb}$ indicates the approximate line spacing of their comb-like rotational spectrum (as estimated in AH14).

This paper is organised as follows. In Section 2 we summarise the calculation of AH14 for the rotational emission of quasi-symmetric planar PAHs and describe the theoretical model and assumptions we rely on to set upper bounds. Our data reduction method is described in detail in Section 4. Section 5 describes our search for combs in our reduced and calibrated data. We derive upper bounds on abundances of individual PAHs in Section 5.2, and conclude in Section 6.

2 THEORETICAL BACKGROUND

In this section we briefly summarise the findings of AH14.

Any rigid rotor is characterised by three moments of inertia $I_1 \leqslant I_2 \leqslant I_3$, to which correspond three rotational constants $A_i \equiv \hbar/(4\pi I_i)$, with dimensions of frequency. The spectrum of a quasi-classical (angular momentum $L \gg \hbar$) triaxial rotor is in general very complex, with a large number of allowed transitions, resulting in a dilution of the radiated energy per transition.

AH14 considered the restricted class of *planar*, *quasi-symmetric* rotors, having in mind nitrogen-substituted symmetric PAHs. For a classical planar rotor, with the third axis perpendicular to the plane, $I_1 + I_2 = I_3$. However, this relation is never exactly satisfied for a quantum-mechanical rotor, and there is always a small but non-zero *inertial defect*

[1] To avoid clutter we shall still call PAH any molecule that derives from an actual PAH (in the rigorous sense of the term) by minor modifications, such as the substitution of C or H atoms by other atoms, or the attachment of a radical on the periphery.

[2] The project ID is GBT/14A-504

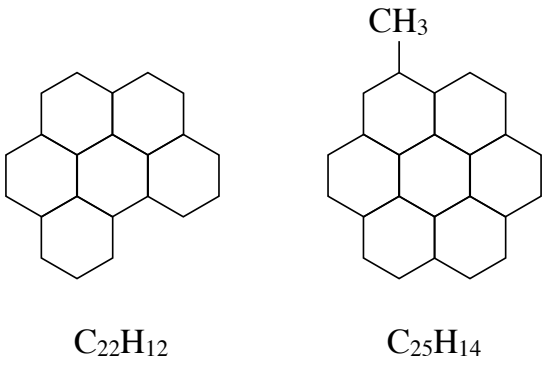

Figure 2. Examples of PAHs or derivatives that *do not qualify* as quasi-symmetric, as the fractional difference between any two of their moments of inertia is larger than a few percent. The rotational spectrum of such large triaxial molecules is complex and diluted among many lines, and we do not attempt to search for them.

$$\delta \equiv 1 - \frac{I_1 + I_2}{I_3}. \quad (1)$$

A perfectly symmetric rotor would have $A_1 = A_2$, and the small departure from this relation is quantified by the asymmetry parameter

$$\epsilon \equiv \frac{A_1 - A_2}{2A_3}. \quad (2)$$

The rotational state of such quasi-symmetric rotors is characterised by two quantum numbers: the total angular momentum J and its projection K along the axis of (quasi)symmetry of the grain, with $-J \leqslant K \leqslant J$. Assuming the electric dipole moment is in the plane of the grain, the strongest transitions are the $(J, K) \rightarrow (J-1, K \pm 1)$. To lowest order in ϵ and δ, the frequency ν_{JK} of the $\Delta K = -1$ transition (or that of the $(J, -K) \rightarrow (J, -K+1)$ transition) is given by (AH14)

$$\begin{aligned} \nu_{JK} &= A_3(4J - 2K + 1) \\ &+ 4A_3\delta(J-K) + \frac{\epsilon^2}{4}A_3(J+K)\left(\frac{J-K}{K}\right)^3. \end{aligned} \quad (3)$$

The power radiated in this transition is

$$P_{JK} = \frac{\mu^2}{6c^3}(2\pi\nu_{JK})^4(1 + K/J)^2, \quad (4)$$

where μ is the electric dipole moment. We see from Eq. (3) that for small asymmetries and inertial defects, the families of transitions with constant $2J - K \equiv J_0$ are clustered around $\nu_{J_0} = A_3(2J_0 + 1)$, reached exactly for $J = K = J_0$. Therefore the spectrum has the appearance of a *comb*, with each "tooth" (labelled by J_0) being a cluster of quasi-coincident lines. If the probability distribution of J peaks around J_0, and given that the power radiated is proportional to $(1 + K/J)^2$, most of the power is radiated for $\frac{2}{3}J_0 \leqslant J \leqslant J_0$, corresponding to $J/2 \leqslant K \leqslant J$, and giving a characteristic relative spread for each cluster[3]

$$\frac{\Delta\nu}{\nu_{J_0}} \approx \frac{2}{3}\delta + \frac{\epsilon^2}{8}. \quad (5)$$

For $\nu_{J_0} \approx 25$ GHz, we find that the width of each cluster is less than our resolution of 0.4 MHz as long as $\delta \lesssim 3 \times 10^{-5}$ and $\epsilon \lesssim 0.01$. AH14 estimated the asymmetry resulting from a single substitution of a carbon atom by a nitrogen atom in coronene and circumcoronene. The resulting values of ϵ are all below 0.01, except for the outermost substitution site in coronene, for which $\epsilon \approx 0.018$. We therefore expect that for most quasi-symmetric nitrogen-substituted PAHs, the asymmetry is small enough to preserve the "comb"-like aspect of the spectrum when observed with 0.4 MHz resolution. It is difficult to estimate the inertial defect of large molecules from first principles. Based on a few measured or computed values for small PAHs, AH14 argued that one can expect it to be of the order of a few parts in 10^5. Provided this estimate is correct, the inertial defect should also be small enough to preserve a "comb" appearance. However, we caution that this is not a robust estimate, and it would be valuable to have accurate computations of the inertial defect of large PAHs.

Finally, we point out that corannulene also has a comb-like spectrum, resulting from transitions $\Delta J = -1, \Delta K = 0$ and an out-of plane electric dipole moment. The frequencies of these transitions are $\nu_J = J \times 1.019685$ GHz (Lovas et al. 2005).

3 OBSERVATIONS

3.1 Choice of target

We have chosen to target the Perseus molecular cloud complex, which has been observed thoroughly at radio and infrared frequencies, and is a well-known source of AME. Using data from the *Planck* satellite complemented by ancillary data from several other experiments, the Planck Collaboration (2011) fit the spectrum of the Perseus cloud with a free-free, dust and AME components. They find an AME contribution of 33.4 ± 4.5 and 31.5 ± 4.4 Jy at 22.8 and 28.5 GHz, respectively, with a FWHM resolution of 1.12 degree. Tibbs et al. (2010) used the Very Small Array (VSA) to carry out observations of the region with higher spatial resolution at 33 GHz, finding a peak flux of 0.2 Jy per 7′ beam. This is consistent with the Planck Collaboration's results, accounting for the loss of power due to the large-scale continuum being resolved out by the VSA interferometer. Recently, Tibbs et al. (2013) used GBT observations at 1.4 and 5 GHz to constrain the amount of free-free emission in the Perseus cloud. They find that free-free emission cannot contribute more than 27% (3σ) of the 33 GHz emission observed by the VSA, confirming its "anomalous" nature. Finally, Tibbs et al. (2013) observed the Perseus cloud at 16 GHz with the Arcminute Microwave Imager (AMI), and found a significant spatial correlation of the emission with infrared emission from small dust grains, strengthening the hypothesis that the AME is indeed due to small spinning dust grains.

We pointed the GBT towards the strongest peak of

[3] AH14 gave a larger analytic estimate of the width of each cluster (Equation 29) because the branch $-J \leqslant K \leqslant -J/2$ was also included there. However, at constant probability distribution for J and K, there is significantly less power radiated in this branch (by two orders of magnitude) than in the $J/2 \leqslant K \leqslant J$ branch, and the estimate we provide here is more accurate.

AME in the Perseus molecular cloud, as measured by Tibbs et al. (2013). The coordinates of the AME peak are RA: 03:44:28.4, Dec: +32:04:42.1 (C.Tibbs, private communication).

3.2 Summary of the observations

Our observations were carried out in five sessions during the month of March 2014, each divided in several scans of approximately half an hour. At the start of each scan, and towards a calibrator near our science target, we measured the telescope focus and pointing offsets in azimuth and elevation. We did not pursue a out-of-focus holography to measure the surface large-scale errors, given the low frequency of our observations. We employed the high-frequency part of the KFPA receiver together with the GBT spectrometer, to obtain the widest possible bandwidth at high spectral resolution. Our observations spanned 3 GHz of bandwidth, from 23.3 to 26.3 GHz, by setting up four partially overlapping 800 MHz-wide widows. Each window was configured to provide 2048 channels with a spectral resolution of 0.390625 MHz. This spectroscopy setup allowed for a single beam on the sky and two circular polarisations to be observed.

The entire set of observations amounted to a total telescope time of 16.75 hours, including 8.7 hours of actual exposure on source and 2.2 hours of exposure on two blank fields off-source. The off-source observations were used for null tests in our analysis. Our observing setup and data calibration (described in the next section) allowed us to reach a sensitivity of 0.4 mJy per 0.4 MHz channel.

4 DATA REDUCTION

4.1 Properties of the raw data

The raw data is given in terms of *count number* $P(n,t)$, as a function of channel number n and time sample t. There are $N_{\rm ch}=2048$ channels per 800 MHz band. Each time sample corresponds to an integration of 2 seconds, split between the four phases described below. The sky frequency (in the local standard of rest) corresponding to channel n is denoted by ν_n. There are two frequency-shifted phases: a "reference" phase and a "signal" phase, differing in sky frequency by a constant shift $\Delta\nu_{\rm fs}=10$ MHz:

$$\nu_n^{\rm sig}=\nu_n^{\rm ref}+\Delta\nu_{\rm fs}. \tag{6}$$

Each of these two phases is itself divided into two subphases, with a calibrating noise diode switched off or on (subscript "cal" for the latter). We denote the raw count numbers for these four phases by $P^{\rm ref}, P^{\rm sig}, P^{\rm ref}_{\rm cal}$ and $P^{\rm sig}_{\rm cal}$, respectively. We show a sample of the raw data in Figure 3.

The raw count numbers are related to the antenna temperature $T_a(\nu)$ of the line emission we are aiming to measure as follows: for each phase ph = ref, sig, we have

$$P^{\rm ph}(n,t) = G^{\rm ph}(n,t)\left[T_a(\nu_n^{\rm ph})+T_{\rm sys}(\nu_n^{\rm ph},t)\right], \tag{7}$$

$$P^{\rm ph}_{\rm cal}(n,t) = G^{\rm ph}(n,t)\left[T_a(\nu_n^{\rm ph})+(T_{\rm sys}+T_{\rm cal})(\nu_n^{\rm ph},t)\right], \tag{8}$$

$$G^{\rm ph}(n,t) = G_{\rm IF}(n,t)G_{\rm RF}(\nu_n^{\rm ph},t). \tag{9}$$

In these equations, the intermediate-frequency gain $G_{\rm IF}$ is the system gain after the local oscillator (where the frequency switching is done) in the optical path. It is identical for the reference and signal phases, up to small variations that may occur during the 1-second lag between them. The radio-frequency gain $G_{\rm RF}$ represents the system gain before the local oscillator, and may differ slightly between the two phases. $T_{\rm sys}$ denotes the total system temperature, including the continuum emission from the observed region. $T_{\rm cal}$ is the temperature of the calibrating noise diode, assumed to be well known and constant over each one of the four 800 MHz sub-bands (and slightly different for each polarisation state), see Bryerton (2011) for a description. The assumed calibrator temperature pairs for each band are, in Kelvins: $\hat{T}_{\rm cal}=(3.243,3.285),(3.733,3.841),(4.341,4.429),(4.791,4.871)$.

The gain has mostly large-scale fluctuations in the frequency domain due to standing waves in the optical path. The largest-scale fluctuations are well visible in Fig. 3. On the other hand, ideal thermal noise is uncorrelated from one channel to another and fluctuate with equal power on all scales, with a variance given by the radiometer equation

$$\langle\delta T_{\rm sys}^2\rangle=\frac{T_{\rm sys}^2}{\Delta\nu_{\rm res}\Delta t}, \tag{10}$$

where $\Delta t\approx 0.4$ s is the exposure time per phase.

These behaviours are better illustrated in Fourier space. We define our Fourier convention as follows: for a function $P(n)$ of channel number, the Fourier transform $\tilde{P}(u)$ is defined for $u=0,...N_{\rm ch}/2$ as

$$\tilde{P}(u)\equiv\frac{1}{N_{\rm ch}}\sum_{n=0}^{N_{\rm ch}-1}P(n)\exp\left(-i\frac{2\pi}{N_{\rm ch}}un\right). \tag{11}$$

The power spectrum of the raw count number is obtained by averaging $2|\tilde{P}(u;t)|^2$ over the few hundred integrations of a given scan. It gives the contribution to the variance of the count number from fluctuations with period $\Delta n=N_{\rm ch}/u$ channels.

The upper (black) line in Fig. 4 shows the power spectrum of the reference phase. We see that fluctuations on small frequency scales have a flat power spectrum, as expected from thermal noise. On large scales $u\lesssim 100$, non-thermal gain fluctuations dominate the power spectrum. The lower (blue) line shows the power spectrum of the difference $(\text{sig}-\text{ref})/\sqrt{2}$. We see that this combination eliminates a substantial part of large-scale gain fluctuations. However, there are still significant non-thermal fluctuations due to the imperfect cancellation of the RF gain between the two phases.

Armed with this basic understanding of the properties of the data, we now describe our data reduction method.

4.2 Data reduction method

4.2.1 Elimination of glitches

Our first step in the data analysis is to identify glitches in the time evolution of each channel. We first compute the local average of the count number by smoothing it over 100 channels in time (we use a Savitsky-Golay smoothing kernel). We then discard any data that differs from this smoothed count number by more than 7 times the expected rms thermal noise fluctuation. We inspect visually all scans that show a large number of flagged data points. We find three distinct cases of large gain fluctuations:

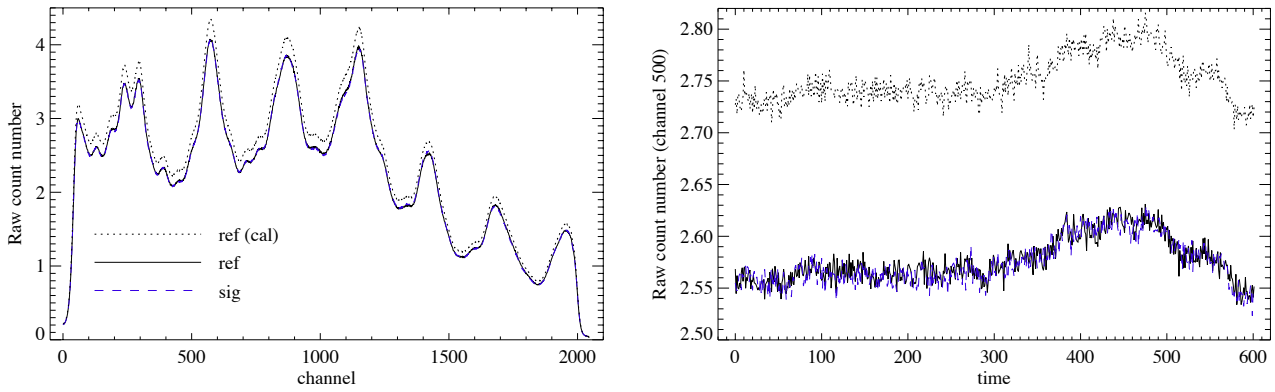

Figure 3. Raw count numbers for the lowest 800 MHz band of the first scan, in one polarisation state. *Left panel:* single time sample as a function of channel number. *Right panel:* Evolution of channel 500 as a function of time (a unit increment on the x-axis corresponds to approximately 2 seconds of actual time).

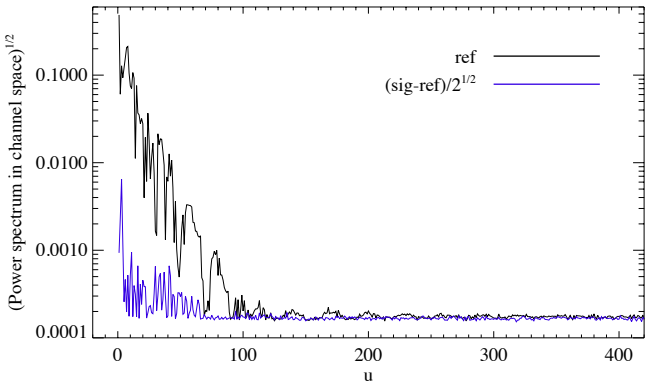

Figure 4. Square root of the power spectrum of the count number for a given scan for the reference and signal phases separately, and for their normalised difference. The variable u corresponds to fluctuations with period $\Delta n = N_{\rm ch}/u$ channels.

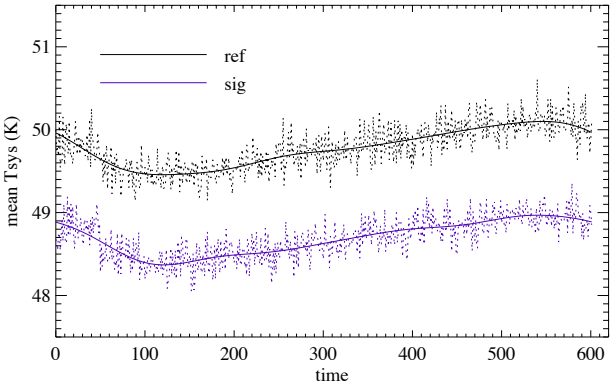

Figure 5. Estimate of the system temperature for the reference (upper, black lines) and signal (lower, blue lines) phases, averaged over the innermost 90% of the band. The solid lines show the slow, non-thermal evolution of the system temperature with time. The $\sim 2\%$ difference between the two phases is systematic across all scans and bands and is likely due to a slight mis-calibration. It has no effect on our analysis.

(i) Transient radio-frequency interference, due to passing satellites. These events are brief (typically lasting a few tens of seconds) and are visible in both polarisations. Even though these glitches are localised in frequency they are so large in amplitude that they affect a broad range of channels. We simply discard all the channels of the affected band during the duration of the glitch.
(ii) Large gain instabilities, often limited to a single polarisation, and lasting for a whole scan. We discard the whole scan from the affected polarisation and bands.
(iii) Detector resonances, taking the form of large glitches in evenly spaced channels ($n = 255 + i \times 256$), and in both the reference and signal phases. We just discard the corrupted channels when this is the case.

4.2.2 Estimation of the system temperature

We estimate the system temperature for each of the two phases as follows:

$$\hat{T}^{\rm ph}_{\rm sys}(n,t) \equiv \hat{T}_{\rm cal} \frac{P^{\rm ph}(n,t)}{P^{\rm ph}_{\rm cal}(n,t) - P^{\rm ph}(n,t)}. \qquad (12)$$

This estimate is noisy, with a fractional error of the order of $\delta T_{\rm sys}/T_{\rm cal}$. Since we only have estimates of the mean calibrator temperature across each band, we can only hope to estimate a mean system temperature as well. We therefore average $\hat{T}_{\rm sys}$ over the innermost 90% of the band. The resulting mean system temperature (typically of the order of 50 K) is shown with dashed lines in Fig. 5 as a function of time. Besides remaining thermal fluctuations of order $\delta T_{\rm sys}/T_{\rm cal}/\sqrt{N_{\rm ch}}$, there are also larger systematic variations on timescales of a few minutes. We keep the first five modes of the time Fourier transform of $\hat{T}_{\rm sys}(t)$ as our final estimate for the mean system temperature. This is shown with solid lines in Fig. 5.

4.2.3 Estimation of the antenna temperature

Our basic approach to eliminate the gain relies on baseline fitting in Fourier space. We denote by $\overline{P}(n,t)$ the count number smoothed in channel space and $\delta P \equiv P - \overline{P}$ the complementary, rapidly fluctuating part. The smoothing is done by keeping the Fourier modes $u \leqslant u_0 \equiv 200$ only, using a hyperbolic tangent with width $\Delta u = 20$ as a truncating function. Our estimate of the antenna temperature for each

phase is then

$$\hat{T}_a^{\rm ph} \equiv \hat{T}_{\rm sys}^{\rm ph}\frac{\delta P^{\rm ph}}{\overline{P}^{\rm ph}}, \quad (13)$$

$$\hat{T}_{a,{\rm cal}}^{\rm ph} \equiv (\hat{T}_{\rm sys}^{\rm ph}+\hat{T}_{\rm cal})\frac{\delta P_{\rm cal}^{\rm ph}}{\overline{P}_{\rm cal}^{\rm ph}}, \quad (14)$$

with noise of variance $T_{\rm sys}^2/\Delta t\Delta\nu_{\rm res}$ and $(T_{\rm sys}+T_{\rm cal})^2/\Delta t\Delta\nu_{\rm res}$, respectively. We average these two estimates with an inverse-variance weighting, and then similarly average the result over all integrations of each scan.

We show the resulting spectrum for the reference phase in Fig. 6, in channel space and in Fourier space, after truncating it outside of the 90% innermost channels with a smooth truncating function. The left plot clearly shows large spikes at a few evenly spaced channels ($n = 255 + i \times 256$), which translate into a dense comb in Fourier space. These channels correspond to the peaks of the standing waves in the gain. In this case theses channels did not show any anomalous behaviour in the time evolution of the gain and were therefore not flagged in the preliminary analysis. The Fourier transform also shows a large spike at $u = 327$, corresponding to standing waves with very short period $\Delta\nu = 2.44$ MHz. These spikes are clearly undesirable high-frequency gain fluctuations that were not eliminated by the smoothing.

Since these features are due to the IF gain, they are cancelled by frequency-switching, i.e. subtracting the reference from the signal phase. This is illustrated in Fig. 7, where we can see that the difference spectrum $T_a^{\rm sig}-T_a^{\rm ref}$ is consistent with thermal noise (besides the truncation at $u \lesssim 200$).

The difference spectrum is then averaged over the two polarisation states and all scans of a given session, with a minimum variance weighting.

While it is critical to eliminate gain contamination from our estimate of the antenna temperature, it is also in our interest to keep as many modes as possible as usable data. Indeed, partial truncation of Fourier modes at u_0 leads to a reduction of the amplitude of the signal, by an amount $2u_0/N_{\rm ch} \approx 20\%$. The variance of the noise is also reduced (and it becomes correlated), but only by the square root of the latter fraction. We have checked that it is not possible to use a truncation value smaller than $u_0 = 200$ without suffering from RF gain contamination at $u \sim 100-200$, which cannot be eliminated by frequency switching. This is illustrated in the spectrum shown in Fig. 8, estimated using a cutoff at $u_0 = 150$ instead of 200. Note that the RF gain fluctuations were not visible in Fig. 4, which showed the average power spectrum of a single integration. Averaging over a few hundred integrations decreases the white noise plateau, to the point where it becomes dominated by the high-frequency tail of the RF gain fluctuations at $u \lesssim 200$.

4.2.4 Calibration

In order to convert the estimated antenna temperature to a flux, we have observed the quasar 3C48. Perley & Butler (2013) provide the following fit for its spectral density flux, as of January 2012:

$$\log_{10}(S_\nu[{\rm Jy}]) = 1.3324 - 0.769\log_{10}(\nu_{\rm GHz})$$

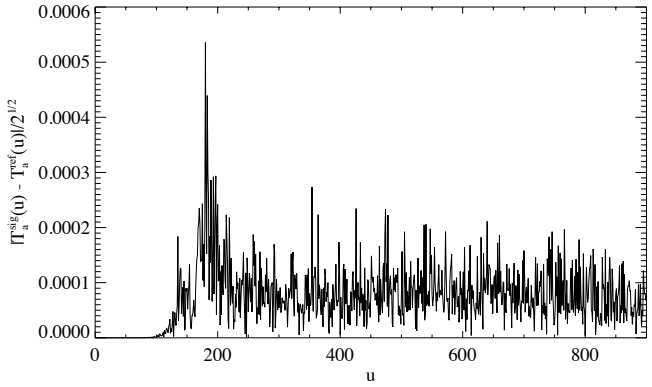

Figure 8. Incomplete elimination of gain fluctuations when using a too gentle cutoff (in this case $u_0 = 150$ instead of 200). Modes $u \approx 150-200$ are significantly contaminated by RF gain fluctuations, which are not cancelled by frequency switching.

$$-0.195[\log_{10}(\nu_{\rm GHz})]^2 + 0.059[\log_{10}(\nu_{\rm GHz})]^3. \quad (15)$$

This translates to mean fluxes of 1.148, 1.114, 1.082 and 1.052 Jy, respectively, when averaging over the central 80% of each one of our four bands.

We have observed 3C48 once per session (except for the first session), and obtained the mean brightness temperature in each band by differentiating the mean system temperature measured on source and off source. Dividing by the known fluxes, we find sensitivities between 1.3 and 1.85 K/Jy, varying between observing sessions and bands[4]

For the first session, where the calibrator was not observed, we estimate the conversion factor T/S_ν by its average over the four remaining sessions.

The final estimate of the flux (or rather of $\Delta S(n)$, the difference between signal and reference phases) is obtained by an inverse-variance averaging of our five observing sessions.

4.2.5 Additional cleaning

After obtaining the reduced and calibrated spectra, we clean the data further as follows:

(*i*) We truncate the band edges where the gain is low and the estimated flux is noisy: typically, we remove 50-100 channels (20-40 MHz) on either side of each band.

(*ii*) We eliminate regions showing strong non-thermal contamination. The highest frequency band is the most affected, with very large contamination near 25.69 GHz, affecting nearly 40% of the band. This contamination is most likely due to a gain issue: it is present in both polarisations but with significantly different amplitudes.

(*iii*) We re-smooth the data in Fourier space and discard modes $u \leqslant 220$, corresponding to fluctuations with period larger than 9.3 channels or 3.6 MHz. The highest-frequency band also shows non-thermal contamination for very high

[4] This analysis did not account for the change in atmospheric opacity from one session to another nor for the change in path-length through the atmosphere during each session. We have computed the total atmospheric opacity and found that the resulting error in calibration is at most 10%. Such corrections can therefore be safely ignored.

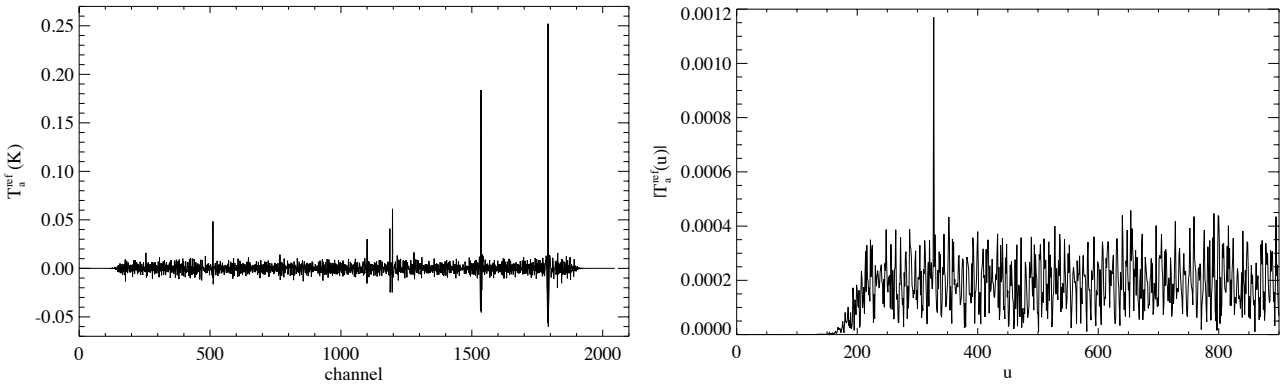

Figure 6. Spectrum of the reference phase averaged over one scan, in channel space (left panel), and in Fourier space (right panel), see description in Sec. 4.2.3.

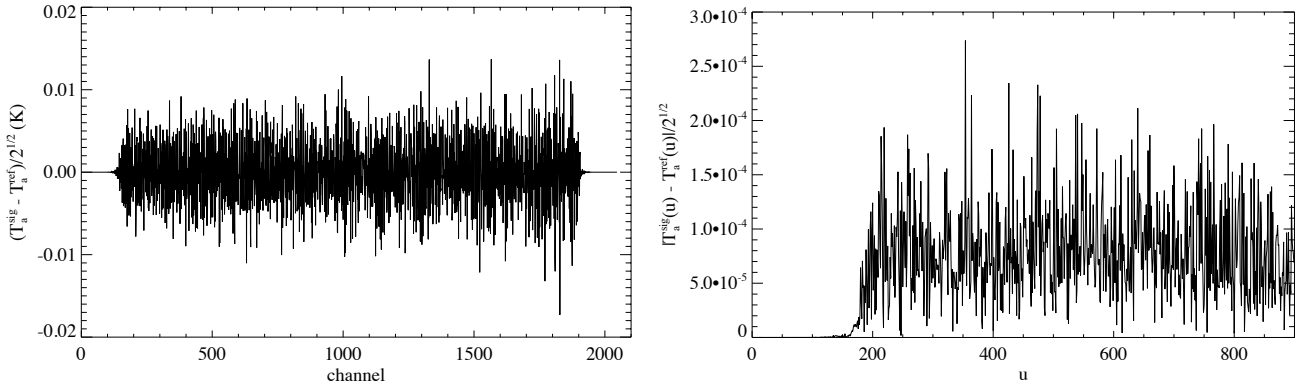

Figure 7. Differential spectrum $(T_a^{\rm sig} - T_a^{\rm ref})/\sqrt{2}$ in channel space (left panel), and in Fourier space (right panel). This combination eliminates the undesirable high-frequency gain fluctuations seen in each phase alone (compare to Fig. 6).

frequency modes ($u \approx N_{\rm chan}/2$). These high-frequency fluctuations are due to the large feature near 25.69 GHz, and we filter them out.

4.2.6 Final reduced spectrum

The final estimate of the flux $\hat{S}(\nu)$ is obtained by the combination

$$\hat{S}(\nu) = \frac{\Delta S(n^{\rm sig}) - \Delta S(n^{\rm ref})}{2}, \qquad (16)$$

where $n^{\rm sig}$ is the channel such that $\nu = \nu_n^{\rm sig}$ (within a channel width), and similarly for $n^{\rm ref}$, so that

$$\hat{S}(\nu) = S(\nu) - \frac{S(\nu + \Delta\nu_{\rm fs}) + S(\nu - \Delta\nu_{\rm fs})}{2} + \text{noise}. \qquad (17)$$

We show our final reduced spectrum $\hat{S}(\nu)$ in Fig. 9.

We have reached noise levels of 0.39 - 0.43 mJy (1σ) per channel, in each of the four 800 MHz bands. The spectrum is consistent with thermal noise.

We detect an intense line at 23.862 GHz, with a flux of 3.6 mJy. This line also appears with high signal-to-noise in the spectrum of the blank field off source (see Fig. 10), and therefore does not originate from the source. We attribute it to atmospheric ozone emission (Gora 1959). We also detect a weaker but still intense feature at 23.87 GHz, in both on and off-source spectra (see Fig. 10). We mask both of these features in the PAH line search. We checked that besides these two features, no strong line in the on-source spectrum also appears at more than 2 sigma in the off-source spectrum.

5 DATA ANALYSIS

5.1 Search for PAH combs

We search for combs in the data of the form $\nu_J = (J + 1/2)\Delta\nu_{\rm comb}$, where J is an integer and $\Delta\nu_{\rm comb}$ is a fixed comb spacing. The signal-to-noise ratio (SNR) for a comb with spacing $\Delta\nu_{\rm comb}$ is simply obtained by summing the intensities at the expected comb frequencies, and normalising by the noise rms fluctuation times the square-root of the number of lines within the bandwidth.

Two combs with spacings $\Delta\nu_1$ and $\Delta\nu_2$ are not differentiable if their spacings are close enough, due to the finite resolution of the data. The combs are distinguishable if $\Delta\nu_J = \nu_J \times \Delta\log(\Delta\nu_{\rm comb}) \geqslant \Delta\nu_{\rm res}$, that is if

$$\Delta\log(\Delta\nu_{\rm comb}) \gtrsim \frac{\Delta\nu_{\rm res}}{\nu} \approx 1.5 \times 10^{-5}. \qquad (18)$$

We use a step $\Delta\log(\Delta\nu_{\rm comb}) = 10^{-6}$ to make sure we do not miss any resonance.

We have computed the SNR for combs with spacings $\Delta\nu_{\rm comb} = 20$ MHz to 600 MHz, corresponding to PAHs with approximately 15 to 100 carbon atoms, and including the expected spacing for coronene and circumcoronene

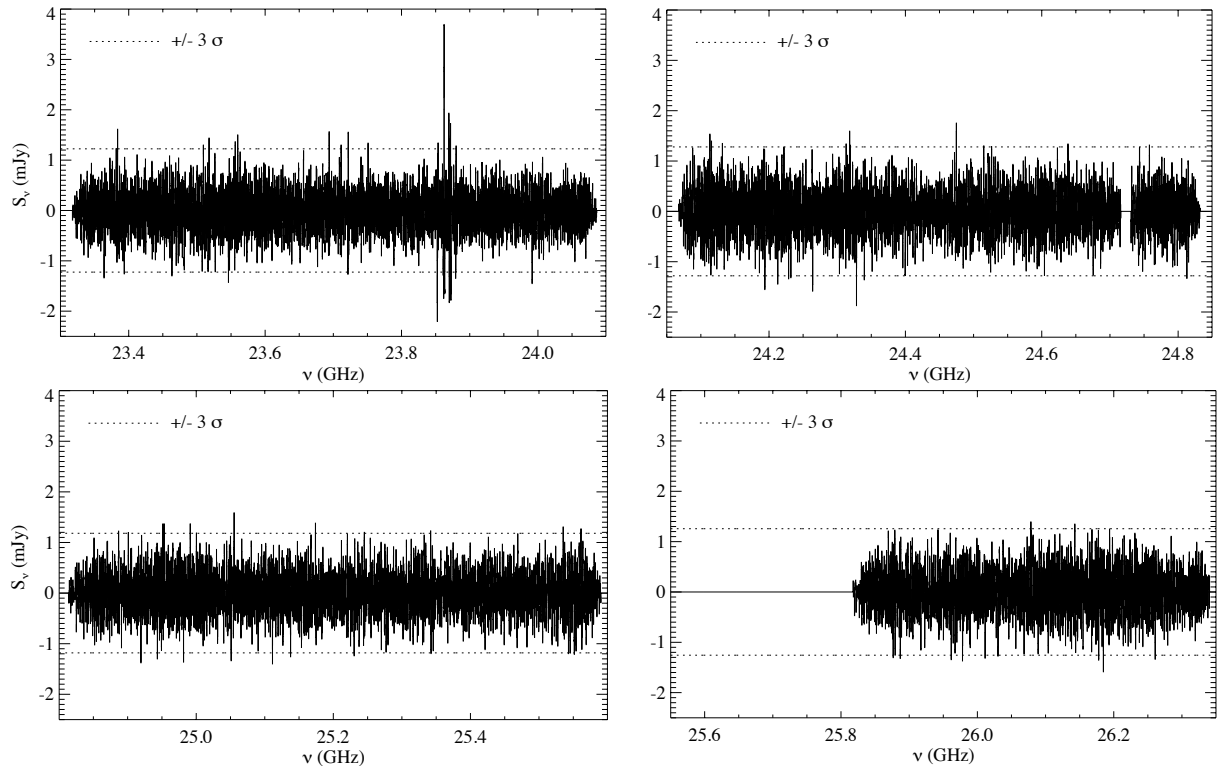

Figure 9. Final reduced and calibrated flux for each one of our four 800 MHz bands – specifically, this is an estimate of $S(\nu) + [S(\nu + 10\ \mathrm{MHz}) - \mathrm{S}(\nu - 10\ \mathrm{MHz})]/2$. The dashed lines show the $\pm 3\sigma$ bands, at approximately ± 1.2 mJy. The blanked regions are discarded data due to large contamination. The strong feature at $\nu = 23.86$ GHz is likely due to ozone emission and is masked during the PAH line search. The negative satellite features at ± 10 MHz are due to the frequency switching.

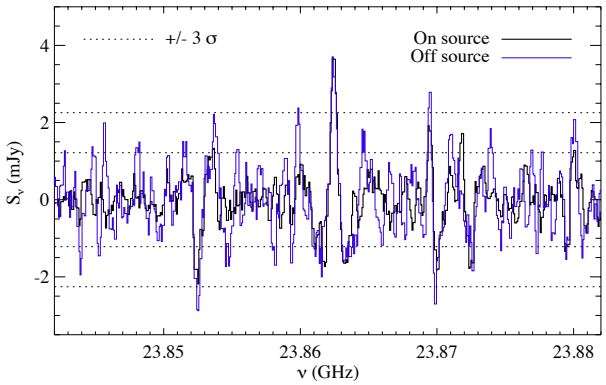

Figure 10. Detail of the spectrum around 23.86 GHz, for our observations on source (black, thick line) and off-source (blue, thin lines). The dashed lines show the $\pm 3\sigma$ boundaries for the two spectra (the noise for the off-source observations is approximately twice larger than that of the on-source observations). The ozone line appears clearly in both spectra as a trong positive feature at $\nu \approx 23.862$ GHz and two negative satellites at ± 10 MHz due to frequency switching. The immediate negatives surrounding the main feature (and positives surrounding the negative satellites) result from high-pass filtering in Fourier space when reducing the data. Finally, a strong feature also appears at 23.87 GHz, in both spectra, and we also mask it for the PAH line search.

($\Delta\nu_{\mathrm{comb}} \approx 340$ and 70 MHz, respectively). The result is shown in Fig. 11. We find that it is consistent with a random noise with zero mean and unit variance. We find several values with SNR > 4, and 1 comb spacing reaching a SNR of 5.2 (for $\Delta\nu = 61.66$ MHz). However their number is roughly consistent from what one expects to find by chance when sampling a gaussian distribution such a large number of times (several times 10^5 uncorrelated samples). Moreover, we find negative SNR values approximately as often as positive ones (in particular, we also find a large negative SNR = -5.7 for $\Delta\nu = 224.22$). As a null test, we ran the same analysis on the spectrum measured in the off position, and found a comparable number of comb spacings with SNR $>$ 4, and two values with SNR > 5 in absolute value.

We therefore conclude that the outcome of our comb search is consistent with pure noise, and that no PAH combs were detected in our data within our sensitivity.

We also searched for the three corannulene lines within our bandwidth and found an overal SNR consistent with noise.

A potential caveat of our analysis is that we assumed PAH lines to be narrower than our resolution. This need not be the case in principle: if the asymmetry parameter and inertial defects are close to or larger than their critical values, or if broadening by turbulent motions is significant (with turbulent velocities larger than 5 km/s corresponding to 0.4 MHz broadening), the lines could be a few channels wide. However, since, we do not know the exact shape of these lines, and moreover smoothing in Fourier space reduces the amplitude of broad features, we have not attempted to search for combs with broader "teeth".

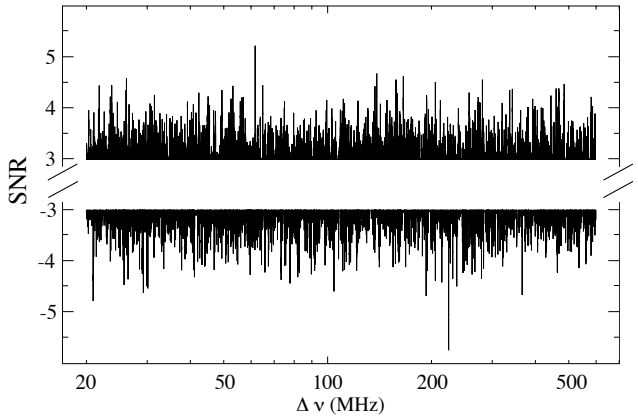

Figure 11. Signal-to-noise ratio (SNR) as a function of comb spacing $\Delta\nu$. Given the very large number of comb spacings sampled (several millions), we only show the points with $|\mathrm{SNR}| > 3$ for the sake of clarity. The number of comb spacings with $|\mathrm{SNR}| > 4$ and $|\mathrm{SNR}| > 5$ is consistent with what we find when carrying the same analysis on the off-source spectrum.

5.2 Implications for PAH abundances

5.2.1 Modelling the expected emission

In order to predict the expected spectrum in the observed bandwidth, we also require a prescription for the probability distribution $\mathcal{P}(J, K)$ for the rotational state of the considered PAH. The theoretical framework for computing this distribution, extending the work of Draine & Lazarian (1998), is now well developed (Ali-Haïmoud et al. 2009; Hoang et al. 2010; Ysard & Verstraete 2010; Hoang et al. 2011; Silsbee et al. 2011; Ali-Haïmoud 2013). We could therefore in principle, given the physical conditions in the observed region, and given the electric dipole moment and asymmetry parameter of any specific PAH, predict its rotational spectrum. This prediction could then be used to set upper bounds on the column density of the considered PAH. Given the large number of parameters involved and our limited knowledge of their values, however, we have chosen not to take this route in this work.

Instead, and following AH14, we shall rely on the observed AME spectrum in the Perseus molecular cloud, and assume that this emission is entirely due to spinning dust radiation. We shall further assume that any specific PAH whose abundance we seek to constrain has a rotation state and dipole moment similar to those of the "typical" PAHs responsible for the AME continuum. This is clearly not strictly correct, as the dipole moments of different nitrogen-substituted circumcoronene, for example, vary by a factor as large as 7 (Hudgins et al. 2005). Moreover, the magnitude of the dipole moment strongly affects the power radiated as well as the peak of the emission (see for example Section 10 of Ali-Haïmoud et al. 2009). While imperfect, this assumption has however the merit of simplicity.

Assuming the rotational emission of a particular PAH is an ideal comb when observed with our finite resolution (i.e. assuming δ and ϵ are small enough), we have:

$$S_\nu^{\mathrm{PAH}} \approx \frac{N_{\mathrm{PAH}}}{N_{\mathrm{PAH,tot}}} \frac{\Delta\nu_{\mathrm{comb}}}{\Delta\nu_{\mathrm{res}}} S_\nu^{\mathrm{AME}}. \tag{19}$$

In the above equation, S_ν^{AME} is the continuum AME flux, which we shall estimate below from existing observations, S_ν^{PAH} is the flux from a specific PAH in each comb "tooth", N_{PAH} is the column density of this PAH, and $N_{\mathrm{PAH,tot}}$ is the total column density of all "typical" PAHs causing the AME.

The 32 Jy AME flux measured by the Planck Collaboration with a resolution of 1.12 degree corresponds (assuming a uniform flux accross their beam) to a flux $S_\nu^{\mathrm{AME}} \approx 1.8$ mJy per 0.5' GBT beam. We shall use this estimate as our fiducial value in Eq. (19). With $\Delta\nu_{\mathrm{res}} = 0.3907$ MHz, we obtain

$$S_\nu^{\mathrm{PAH}} \approx 0.45 \text{ mJy } \frac{N_{\mathrm{PAH}}}{0.001\ N_{\mathrm{PAH,tot}}} \frac{\Delta\nu_{\mathrm{comb}}}{100 \text{ MHz}}. \tag{20}$$

5.2.2 Upper bounds on abundances of specific PAHs

Given our reached sensitivity $\sigma = 0.4$ mJy, we can set upper bounds on the abundance of specific PAHs towards Perseus. We do not reach a SNR larger than 5 in our comb search; this implies that

$$\frac{S_\nu^{\mathrm{PAH}}}{0.4 \text{ mJy}} \sqrt{\frac{\Delta\nu_{\mathrm{tot}}}{\Delta\nu_{\mathrm{comb}}}} \leqslant 5. \tag{21}$$

Using Eq. (20) to relate the flux in a particular comb to the fractional abundance of the underlying PAH, decreased by 20% to account for filtering in Fourier space, we derive the approximate limit

$$\frac{N_{\mathrm{PAH}}}{N_{\mathrm{PAH,tot}}} \lesssim 0.001 \sqrt{\frac{100 \text{ MHz}}{\Delta\nu_{\mathrm{comb}}}}. \tag{22}$$

The numerical value of the right-hand side only varies by a factor of a few between coronene-sized grains ($\Delta\nu_{\mathrm{comb}} \approx 340$ MHz) and circumcoronene-sized grains ($\Delta\nu_{\mathrm{comb}} \approx 70$ MHz).

We emphasise that here by specific PAH we mean a molecule uniquely determined by its matrix of inertia. For example, singly ionized nitrogen-substituted coronene, with nitrogen in the innermost benzene ring, only ^{12}C atoms, and no deuterium substitution, qualifies as a specific PAH. Two forms of nitrogen-substituted coronene, with the same chemical formula but substitution sites that give rise to different moments of inertia, would on the other hand be considered as two different specific PAHs. If one wishes to set an upper bound on the total abundance of, for example, all derivatives of coronene, we need a prescription for the fraction of coronene in any particular specific variant. AH14 estimated such fractions to be ~ 6 percent and ~ 1.6 percent for coronene and circumcoronene, respectively, assuming two charge states, a nitrogen substitution rate (i.e. the ratio of N to C atoms in PAHs) of 3 per cent, and a ^{12}C/^{13}C ratio of 70. Besides, AH14 assumed negligible rates of super- or dehydrogenation, neglected possible methyl or ethyl side groups that may be attached to PAHs (Li & Draine 2012), and assumed a negligible rate of deuterium substitution. The latter assumption could be significantly inaccurate: Draine (2006) and Linsky et al. (2006) argued that PAHs could be heavily deuterated, with D/H fractions in PAHs possibly reaching several percent. The quoted fractions of 6 and 1.6 percent should therefore rather be considered as upper bounds, keeping in mind that the variety within each PAH "family" could be significantly larger.

Using these values, we find an upper bound on all forms of coronene of approximately

$$N_{\rm coronene,tot} \lesssim 0.01\ N_{\rm PAH,tot}, \quad (23)$$

and a bound approximately 10 times weaker for circumcoronene:

$$N_{\rm circumcoronene,tot} \lesssim 0.1\ N_{\rm PAH,tot}. \quad (24)$$

We conclude this section by recalling that many assumptions have been used to derive these bounds, some rather optimistic:
(*i*) We have assumed that the spectrum of the searched PAHs peaks around $\sim 20-30$ GHz, like the AME spectrum; in reality, it could be that quasi-symmetric PAHs have a significantly larger or smaller dipole moment than the fiducial population, and that their emission peaks at significantly lower or higher frequencies. The gain in power due to a larger dipole moment may not be enough to compensate for the exponential fall of the distribution function of angular momenta beyond its peak.
(*ii*) We do not have a good handle of the inertial defect of large planar PAHs. The comb-like aspect of the rotational emission would be destroyed if the inertial defect was significantly larger than a few parts in 10^5.
(*iii*) We have assumed that the amount of impurities on PAHs is rather low, and neglected deuterium substitutions and the attachment of side groups. This biases the conversion from the abundance of a specific PAH (determined uniquely by its inertia tensor), which is what is directly constrained here, to the overall abundance of the "mother PAH", including all of its derivatives.
(*iv*) We have assumed that turbulent broadening is negligible, i.e. that turbulent velocities along the line of sight are less than ~ 5 km/s, beyond which lines would spread across several channels.

6 CONCLUSION

We have searched for comb-like rotational emission from quasi-symmetric "grand PAHs" in the Perseus molecular cloud, a region known to harbour AME, most probably caused by spinning PAHs. We conducted this search by match-filtering spectroscopic data acquired with the Green Bank Telescope. Our data reduction method relies on smoothing in Fourier space and frequency switching in order to eliminate gain fluctuations. We have reached a noise level of 0.4 mJy per 0.4 MHz channel, over a total bandwidth of 3 GHz.

This noise level was not sufficient to make a detection, but allowed us to set informative upper bounds on the abundance of specific, quasi-symmetric PAHs, provided the AME observed in Perseus is primarily due to small spinning dust grains. In addition, our upper bounds generically apply to a large range of PAHs, with $\sim 15-100$ carbon atoms.

Our upper bounds imply that any specific charge state and substitution state of a quasi-symmetric PAH cannot make more than $\sim 0.1\%$ of the the total PAH population. This in turn implies that the total amount of any quasi-symmetric PAH (i.e. including all charge and substitution states) is at most a few percent of the total PAH population. These bounds should be used with caution, however, as they rely on assuming that the constrained specific PAHs have similar properties as the fiducial PAHs producing the spinning dust emission.

Our non-detection of specific PAHs could very well result from a non-optimal choice of target or frequency domain, and more searches are warranted, exploring other regions of the sky with different instruments and at different wavelengths. Identifying specific PAHs would be an important milestone in our understanding of the ISM. In this work we have used a new and promising technique, and hope to have paved the way for more searches to come.

ACKNOWLEDGEMENTS

We are grateful to the GBT staff for their availability during our visit and to Dan Perera for help with preliminary data reduction. We also thank Bruce Draine for detailed comments on this manuscript and Clive Dickinson and Christopher Tibbs for useful discussions.

Y.A.-H. was supported by the Frank and Peggy Taplin fellowship while at the Institute for Advanced study, and is supported by the John Templeton Foundation award 43770 at the Johns Hopkins University. The National Radio Astronomy Observatory is a facility of the National Science Foundation operated under cooperative agreement by Associated Universities, Inc.

REFERENCES

Ali-Haïmoud Y., 2013, Advances in Astronomy, 2013, 462697
Ali-Haïmoud Y., 2014, MNRAS, 437, 2728
Ali-Haïmoud Y., Hirata C. M., Dickinson C., 2009, MNRAS, 395, 1055
Allamandola L. J., Tielens A. G. G. M., Barker J. R., 1989, Astrophys. J. Suppl. Ser., 71, 733
Bryerton E. W., 2011, IEEE Transactions on Microwave Theory Techniques, 59, 2117, 1106.0944, ADS
Draine B. T., 2006, in Sonneborn G., Moos H. W., Andersson B.-G., eds, Astrophysics in the Far Ultraviolet: Five Years of Discovery with FUSE Vol. 348 of Astronomical Society of the Pacific Conference Series, Can Dust Explain Variations in the D/H Ratio?. p. 58, ADS
Draine B. T., Lazarian A., 1998, ApJ, 508, 157
Galazutdinov G., Lee B.-C., Song I.-O., Kazmierczak M., Krełowski J., 2011, MNRAS, 412, 1259
Gora E. K., 1959, Journal of Molecular Spectroscopy, 3, 78
Gredel R., Carpentier Y., Rouillé G., Steglich M., Huisken F., Henning T., 2011, A&A, 530, A26
Hammonds M., Pathak A., Candian A., Sarre P. J., 2011, in Joblin C., Tielens A. G. G. M., eds, EAS Publications Series Vol. 46 of EAS Publications Series, Spectroscopy of Protonated and Deprotonated PAHs. pp 373–379
Hoang T., Draine B. T., Lazarian A., 2010, ApJ, 715, 1462
Hoang T., Lazarian A., Draine B. T., 2011, ApJ, 741, 87
Hudgins D. M., Bauschlicher Jr. C. W., Allamandola L. J., 2005, ApJ, 632, 316
Iglesias-Groth S., González Hernández J., Manchado A., 2012, MNRAS, 420, 2785
Iglesias-Groth S., Manchado A., García-Hernández D. A., González Hernández J. I., Lambert D. L., 2008, ApJ, 685, L55

Iglesias-Groth S., Manchado A., Rebolo R., González Hernández J. I., García-Hernández D. A., Lambert D. L., 2010, MNRAS, 407, 2157
Kwok S., Zhang Y., 2011, Nature, 479, 80
Kwok S., Zhang Y., 2013, ApJ, 771, 5
Leitch E. M., Readhead A. C. S., Pearson T. J., Myers S. T., 1997, ApJ, 486, L23
Li A., Draine B. T., 2012, ApJ, 760, L35
Linsky J. L., et al., 2006, ApJ, 647, 1106, astro-ph/0608308, ADS
Lovas F. J., McMahon J. R., Grabow J. U., Schnell M., Mack J., Scott L. T., Kuczkowski R. L., 2005, J. Am. Chem. Soc., pp 4345–9
Mulas G., Malloci G., Joblin C., Toublanc D., 2006, A&A, 460, 93
Perley R. A., Butler B. J., 2013, Astrophys. J. Suppl. Ser., 204, 19
Pilleri P., Herberth D., Giesen T. F., Gerin M., Joblin C., Mulas G., Malloci G., Grabow J.-U., Brünken S., Surin L., Steinberg B. D., Curtis K. R., Scott L. T., 2009, MNRAS, 397, 1053
Rosenberg M. J. F., Berné O., Boersma C., 2014, arXiv e-prints, 1405.5383
Salama F., Galazutdinov G. A., Krełowski J., Biennier L., Beletsky Y., Song I.-O., 2011, ApJ, 728, 154
Silsbee K., Ali-Haïmoud Y., Hirata C. M., 2011, MNRAS, 411, 2750
Thaddeus P., 2006, Phil. Trans. R. Soc. B, p. 16811687
The Planck Collaboration 2011, A&A, 536, A20
Tibbs C. T., et al., 2010, MNRAS, 402, 1969
Tibbs C. T., Paladini R., Dickinson C., Mason B. S., Casassus S., Cleary K., Davies R. D., Davis R. J., Watson R. A., 2013, ApJ
Tibbs C. T., Scaife A. M. M., Dickinson C., Paladini R., Davies R. D., Davis R. J., Grainge K. J. B., Watson R. A., 2013, ApJ
Tielens A. G. G. M., 2008, Annual Rev. Astron. Astrophys., 46, 289
Tielens A. G. G. M., 2013, Reviews of Modern Physics, 85, 1021
Yang X. J., Glaser R., Li A., Zhong J. X., 2013, ApJ, 776, 110
Ysard N., Verstraete L., 2010, A&A, 509, A12